

## Niobium Oxide Photocatalytically Oxidizes Ammonia in Water at Ambient Conditions

Welman C. Elias,<sup>#,a</sup> Chelsea A. Clark,<sup>#,a</sup> Kimberly N. Heck,<sup>a</sup> Jacob H. Arredondo,<sup>a</sup>  
Bo Wang,<sup>a</sup> Andras Toro,<sup>b</sup> László Kürti<sup>b</sup> and Michael S. Wong<sup>✉\*,a,b,c,d,e</sup>

<sup>a</sup>Department of Chemical and Biomolecular Engineering, Rice University,  
6100 Main Street, 77005 Houston-TX, USA

<sup>b</sup>Department of Chemistry, Rice University, 6100 Main Street, 77005 Houston-TX, USA

<sup>c</sup>Department of Civil and Environmental Engineering, Rice University,  
6100 Main Street, 77005 Houston-TX, USA

<sup>d</sup>Department of Materials Science and NanoEngineering, Rice University,  
6100 Main Street, 77005 Houston-TX, USA

<sup>e</sup>Nanosystems Engineering Research Center for Nanotechnology-Enabled Water Treatment,  
Rice University, 6100 Main Street, 77005 Houston-TX, USA

Ammonia contamination in water is a significant environmental issue since it is toxic and leads to eutrophication. Photocatalysis has been investigated as a strategy for ammonia degradation but can potentially form toxic nitrite ( $\text{NO}_2^-$ ) and nitrate ( $\text{NO}_3^-$ ) byproducts. This work reports on the ability of niobium oxide ( $\text{Nb}_2\text{O}_5$ ) to photocatalytically oxidize aqueous-phase ammonia ( $\text{NH}_3$ ). Whereas as-synthesized  $\text{Nb}_2\text{O}_5$  showed little catalytic activity ( $< 1\%$   $\text{NH}_3$  conversion after 6 h of UV-C irradiation, at room temperature and atmospheric pressure, and under  $\text{O}_2$  headspace),  $\text{Nb}_2\text{O}_5$  treated in basic solution ( $\text{OH-Nb}_2\text{O}_5$ ) was able to photocatalytically degrade  $\text{NH}_3$  at ca. 9% conversion after six hours, with ca. 70% selectivity to the desired  $\text{N}_2$ , with a first-order rate constant of ca. 12 times higher than the as synthesized catalyst ( $1.6 \times 10^{-3} \text{ min}^{-1}$  vs.  $2.0 \times 10^{-2} \text{ min}^{-1}$ ). Raman spectroscopic analysis indicated the presence of terminal Nb=O species after base treatment of  $\text{Nb}_2\text{O}_5$ , implicating them as catalytically active sites. These results underscore how a simple structural modification can significantly affect photocatalytic activity for aqueous ammonia oxidation.

**Keywords:** ammonia oxidation, photocatalysis, niobium oxide, aqueous ammonia

### Introduction

Ammonia contamination plays a significant role in the eutrophication and reduction of dissolved oxygen in ground and surface waters, which can result in toxicity to aquatic life at very low concentrations ( $< 1 \text{ mg NH}_3 \text{ L}^{-1}$ ).<sup>1</sup> The largest source of ammonia-containing wastewater is the direct discharge of nutrient-rich animal waste, with other sources such as fertilizer manufacturing, food processing, landfill leachate, and wastewater treatment facilities also contributing to the problem.<sup>2-4</sup> Excess ammonia can also pose a problem during drinking water treatment by

compromising the efficiency of disinfection processes or by conversion into the more toxic species such as nitrite and nitrate.<sup>5</sup>

Current technologies for the remediation of aqueous ammonia pollution include biological denitrification,<sup>6</sup> breakpoint chlorination,<sup>7</sup> and catalytic degradation.<sup>8</sup> Biological denitrification is typically very slow, limited to low ammonia concentrations, and produces sewage sludge as a byproduct. Breakpoint chlorination is widely used in drinking water disinfection; however, it is only practical for low influent concentrations of ammonia and can cause the formation of toxic disinfection byproducts.<sup>5,7</sup> Catalytic treatment approaches are promising due to their lower byproduct formation, nontoxicity, and flexible operation. Most current aqueous ammonia oxidation catalysts require

\*e-mail: mswong@rice.edu

<sup>#</sup>These authors contributed equally to the manuscript

Editor handled this article: Célia M. Ronconi (Associate)



significant energy input in the form of high pressure, temperature, or electricity. Further, current  $\text{NH}_3$  oxidation catalysts suffer from poisoning at low reaction temperatures due to unreactive dehydrogenated  $\text{N}^*$  and  $\text{NH}_x^*$  species on the surface.<sup>8-10</sup>

Advanced photocatalytic oxidation (AOPs) has emerged as a promising and effective technique for the degradation of water contaminants, particularly ammonia.<sup>11-14</sup> The method has several advantages, including a broad operational pH range spanning from 2 to 11, utilization of environmentally friendly chemicals, operational simplicity, cost-effectiveness, and exceptional efficiency in mineralization. However, the inherent challenge lies in the substantial band gap of commonly employed semiconductors, such as titania oxide ( $\text{TiO}_2$ , with an anatase phase band gap of 3.2 eV), which curtails their capacity to absorb visible light. This constraint restricts the use of visible light for catalytic activation. Additionally, certain photocatalysts necessitate UV-C and UV-A light sources to generate crucial reactive species, including hydroxyl radicals ( $\text{HO}\bullet$ ), sulfate radicals ( $\text{SO}_4^{\bullet-}$ ), singlet oxygen ( $^1\text{O}_2$ ), and superoxide anions ( $\text{O}_2^{\bullet-}$ ).<sup>15-17</sup> Furthermore, the availability of natural sunlight is confined to a limited timeframe, thereby imposing a temporal constraint on the use of this technology.

AOPs for ammonia removal from water has been a subject of thorough investigation, particularly concerning catalysts predominantly derived from  $\text{TiO}_2$  and zinc oxide ( $\text{ZnO}$ ). The reaction pH is a critical parameter in affecting the yield and selectivity to dinitrogen ( $\text{N}_2$ ) during  $\text{NH}_3$  photo-oxidation.<sup>14</sup> It has been reported to affect  $\text{NH}_3$  adsorption on the catalyst surface for  $\text{TiO}_2$ -based catalysts, where at acidic pH the elevated concentration of hydronium ions increases the surface exchange competition with ammonium ( $\text{NH}_4^+$ ), with the ideal pH to be between 9.3 (i.e., the  $\text{p}K_a$  of  $\text{NH}_4^+$ ) and 10, due to the more favorable adsorption of neutral  $\text{NH}_3$ . At pH values higher than 10, reaction performance decreases are attributed to the competitive adsorption between hydroxyl anions and  $\text{NH}_3$ .<sup>11-14</sup>

Adding transition metals such as platinum (Pt) to traditional photocatalysts (e.g.  $\text{TiO}_2$ ,  $\text{ZnO}$ ) can also enhance reaction yield and/or selectivity.<sup>14</sup> These enhancements are proposed to be associated with the ability of transition metals to capture  $e^-$  from the conduction band,<sup>14,18-20</sup> and/or better interaction with nitrogenated species.<sup>21</sup> Ou *et al.*<sup>22</sup> showed that the photodegradation of aqueous ammonia over platinized titanate nanotubes (TNTs) increases from 5 to 85% with the addition of 20 wt.% of Pt, which was proposed to be associated with the stronger absorption affinity of Pt with  $\text{NH}_3/\text{NH}_4^+$  than to the unmodified TNTs. While the addition of transition metals generally improves

ammonia photooxidation performance, it also increases photocatalyst cost, especially with the elevated loadings of noble metals required.

$\text{Nb}_2\text{O}_5$  has a similar band gap to the most widely reported photocatalyst  $\text{TiO}_2$  (3.5 eV vs. 3.4 eV, respectively)<sup>23,24</sup> and has been explored as a photocatalyst for carbon dioxide ( $\text{CO}_2$ ) reduction<sup>25</sup> as well as water oxidation.<sup>24</sup> However, to our knowledge, this semiconductor material has never been studied for aqueous ammonia photooxidation. However, it has shown promise in heterogeneous gas-phase ammonia oxidation at elevated temperatures.<sup>26</sup> In this work, we prepared  $\text{Nb}_2\text{O}_5$  and tested it for aqueous ammonia photocatalysis. While the as-prepared material had low activity, we found that a simple base treatment substantially improved the ammonia photooxidation activity. Through Raman spectroscopy, we identified structural features to which we attribute the much higher photooxidation activity of the base-treated material.

## Experimental

### Materials

$\text{NH}_4\text{Cl}$ ,  $\text{NH}_4[\text{NbO}(\text{C}_2\text{O}_4)_2(\text{H}_2\text{O})_2]\cdot n\text{H}_2\text{O}$ ,  $\text{TiO}_2$ -P25, and  $\text{NaOH}$  were all purchased from Sigma-Aldrich (St. Louis, MO, USA). Oxygen (99.999%) was purchased from Airgas (Houston, TX, USA). Deionized water (DI water, 18.2  $\text{M}\Omega$  cm at 25 °C, Thermo Fisher Scientific, Waltham, MA, USA) was used for all experiments.

### Catalyst synthesis

The  $\text{Nb}_2\text{O}_5$  was synthesized following previous reports.<sup>27</sup> Briefly, 4.8 g of ammonium niobium oxalate ( $\text{NH}_4[\text{NbO}(\text{C}_2\text{O}_4)_2(\text{H}_2\text{O})_2]\cdot n\text{H}_2\text{O}$ ) were dissolved in 70 mL of DI water, and placed in a Parr Teflon-lined stainless steel autoclave (Moline, IL, USA) for 24 h at 175 °C. The resultant powder was filtered, washed with 1 L of DI  $\text{H}_2\text{O}$  per gram of material, dried overnight at 80 °C, and then calcined under air at 400 °C for 2 h. This as-synthesized  $\text{Nb}_2\text{O}_5$  was used to prepare a modified  $\text{Nb}_2\text{O}_5$  ( $\text{OH-Nb}_2\text{O}_5$ ) by mixing 2 g of  $\text{Nb}_2\text{O}_5$  with 10 mL of 1 M  $\text{NaOH}$  under vigorous stirring for 2 h at room temperature. The resulting solid was washed with DI water (1 L of DI water per gram of material) and then dried overnight at 80 °C.

### Ammonium photooxidation experiments

Ammonium photooxidation experiments were carried out in an enclosed photoreactor fabricated in-house and described in previous publications,<sup>28-31</sup> equipped with six

UV-C Ushio G4T5 low-pressure mercury lamps (Cypress, CA, USA; primary emission wavelength at 254 nm; input 4 W and output 0.8 W). A 120-mL quartz round-bottom flask was used as a vessel for the reaction. The threads were lined with Teflon tape and then capped with a silicone septum, into which an oxygen purge needle and a gas vent needle were inserted.

In a typical batch experiment, 0.4 g L<sup>-1</sup> of catalyst is loaded into the quartz round bottom bottle, and left to stir for 15 min. The pH of the solution was then adjusted to 9 by the addition of aliquots of NaOH stock solution (1 M and/or 10 M). Next, the system was purged with oxygen at 100 mL min<sup>-1</sup> for ca. 15 min before a concentrated solution of NH<sub>4</sub>Cl (10 g NH<sub>4</sub><sup>+</sup> L<sup>-1</sup>) was injected to obtain a final solution concentration of 75 mg NH<sub>4</sub><sup>+</sup> L<sup>-1</sup> (= 4.2 mmol N L<sup>-1</sup>). The reaction vessel was left to stir in the dark for one hour, after which the UV-C lamps were turned on and the reaction was carried out for a total of 6 h. 1 mL aliquots were taken via syringe over time.

#### Measurement of nitrogen species concentrations

The NH<sub>4</sub><sup>+</sup> concentration in the aqueous phase was measured by ion chromatography (IC, Thermo Fisher Scientific, Waltham, MA, USA) with suppressed conductivity detection (Dionex Aquion, 4 × 250 mm IonPac CS12, CDRS Suppressor at 59 mA) using 20 mM methane sulphonic acid eluent at 1 mL min<sup>-1</sup> flow rate. The limit of detection for this quantification method was 0.1 ppm NH<sub>4</sub><sup>+</sup>. The aqueous NO<sub>3</sub><sup>-</sup> and NO<sub>2</sub><sup>-</sup> concentrations were also measured by IC (Thermo Fisher Scientific, Waltham, MA, USA; Dionex Aquion, 4 × 250 mm IonPac AS23, AERS 500 Carbonate Suppressor at 32 mA) using a carbonate/bicarbonate eluent (10 mL of 0.45 M sodium carbonate, 1 mL of 0.45 M sodium bicarbonate and 989 mL of DI water) at 1 mL min<sup>-1</sup> flow rate. The limits of detection for this quantification method were 0.1 ppm NO<sub>2</sub><sup>-</sup>, and 0.1 ppm NO<sub>3</sub><sup>-</sup>.

#### Materials characterization

Powder X-ray diffraction (XRD) patterns were collected on a Rigaku D/Max Ultima II diffractometer (Tokyo, Japan; 40 kV, 40 mA) using CuK $\alpha$  radiation (1.5418 Å). The data was collected from 15° to 90° at a rate of 2° min<sup>-1</sup> and step size of 0.04°. Scanning electron microscopy (SEM) images were taken on a JEOL 6500F microscope (Tokyo, Japan). The samples were loaded on a carbon tape and analyzed at 15 kV high tension. Brunauer-Emmett-Teller (BET) surface area measurements were performed on an Autosorb-iQ-MP Quantachrome (Boynton Beach, FL, USA) system

measured at liquid-nitrogen temperature (77 K). Prior to the measurements, the samples were degassed for 12 h under vacuum (ca. 2 mmHg) at 200 °C. Raman spectra were taken under *ex-situ* conditions (*i.e.*, room temperature, ambient air) using a Renishaw inVia microRaman spectrometer (New Mills, UK) with a 532 nm excitation laser and a 40× long working distance objective. Spectra were obtained using 0.05 mW power and 10 s integration times. For each sample, five spectra were acquired at different spots and averaged. The standard deviation between spectra for each sample was less than 5%. The absorption spectra of the photocatalysts were determined utilizing diffuse reflectance ultraviolet-visible (DR-UV) spectroscopy. To facilitate measurements, the powders were blended with 60 wt.% BaSO<sub>4</sub>, subsequently compacted into wafers, and analyzed with a Shimadzu UV-2450 spectrometer (Kyoto, Japan). Diffuse reflectance spectroscopy (DRS) profiles were then applied to determine the optical bandgap energy of the samples using Tauc Plot analysis ((F(R)h $\nu$ )<sup>0.5</sup> vs. h $\nu$ ); where h is the Planck's constant,  $\nu$  is the frequency of incident photons, and F(R) is the Kubelka-Munk function.<sup>32</sup>

#### Selectivity and performance comparison

The percent NH<sub>4</sub><sup>+</sup> conversion ( $X_{\text{NH}_4^+}$ ) and the selectivity to NO<sub>2</sub><sup>-</sup> ( $S_{\text{NO}_2^-}$ ) and NO<sub>3</sub><sup>-</sup> ( $S_{\text{NO}_3^-}$ ) were calculated using equations 1, 2 and 3:

$$X_{\text{NH}_4^+} = \frac{[\text{NH}_4^+]_0 - [\text{NH}_4^+]_t}{[\text{NH}_4^+]_0} \times 100 \quad (1)$$

$$S_{\text{NO}_2^-} = \frac{[\text{NO}_2^-]_t}{[\text{NH}_4^+]_0 - [\text{NH}_4^+]_t} \times 100 \quad (2)$$

$$S_{\text{NO}_3^-} = \frac{[\text{NO}_3^-]_t}{[\text{NH}_4^+]_0 - [\text{NH}_4^+]_t} \times 100 \quad (3)$$

where [NH<sub>4</sub><sup>+</sup>]<sub>0</sub>, [NH<sub>4</sub><sup>+</sup>]<sub>t</sub>, [NO<sub>2</sub><sup>-</sup>]<sub>t</sub>, and [NO<sub>3</sub><sup>-</sup>]<sub>t</sub> are species molar concentrations and where the subscript 0 refers to the initial time and t refers to a given time. The selectivity to molecular N<sub>2</sub> ( $S_{\text{N}_2}$ ) (was calculated from the total nitrogen mass balance (equation 4).

$$S_{\text{N}_2} = 100 - (S_{\text{NO}_2^-} + S_{\text{NO}_3^-}) \quad (4)$$

The potential formation of gaseous N<sub>2</sub>O and NO<sub>2</sub> byproducts was verified to not occur in our reaction system via GC-MS measurements.

Performance comparison of various published catalysts for aqueous ammonia photo-oxidation was assessed using quantum yield (QY) and space-time yield (STY)

as proposed and discussed by Vikrant *et al.*<sup>14</sup> (equations 5 and 6).

$$QY = \frac{\text{NH}_3/\text{NH}_4^+ \text{ decay rate (molecules s}^{-1}\text{)}}{\text{photon flux (photon s}^{-1}\text{)}} \quad (5)$$

$$\text{STY} = \frac{QY}{\text{mass of catalyst (mg)}} \quad (6)$$

QY values were calculated based on the peak wavelength of the light source reported. When the wavelength was not specified, the commonly used wavelength for visible light and UV light was applied to calculate the performance (420 and 365 nm, respectively). The photon flux for our enclosed photoreactor was measured to be  $1.2 \times 10^{17}$  photons  $\text{s}^{-1}$  via chemical actinometry, as reported previously.<sup>29</sup>

## Results and Discussion

It has been reported that pH plays an important role in the photo-oxidation of ammonia since in acidic conditions fewer OH<sup>-</sup> anions are present, leading to a much lower generation rate of hydroxyl radicals in the reaction media<sup>33</sup> which are proposed to be active for this reaction,<sup>14</sup> and the ideal reaction pH has been reported to be around 9.<sup>11-14</sup> Since initial screening experiments indicated that the

as-synthesized Nb<sub>2</sub>O<sub>5</sub> was weakly active (Figure 1), we chose to use the modified niobium support (OH-Nb<sub>2</sub>O<sub>5</sub>) to determine how a neutral or basic pH affects the ammonium photo-oxidation reaction. 20 mg of the modified niobium support (OH-Nb<sub>2</sub>O<sub>5</sub>) was added to 50 mL of O<sub>2</sub>-saturated DI water containing 100 mg L<sup>-1</sup> of NH<sub>4</sub><sup>+</sup> (Figure S1, Supplementary Information (SI) section). NH<sub>4</sub><sup>+</sup> degradation did not occur without illumination. Almost no conversion of ammonia to NO<sub>2</sub><sup>-</sup> and NO<sub>3</sub><sup>-</sup> was observed at pH 7, but a 15-fold increase in NH<sub>4</sub><sup>+</sup>/NH<sub>3</sub> conversion and a 5-fold increase in NO<sub>2</sub><sup>-</sup> and NO<sub>3</sub><sup>-</sup> formation was observed when the pH was raised to 9.

After confirming the ideal reaction pH to be 9 (Figure S1), we compared the OH-Nb<sub>2</sub>O<sub>5</sub> photocatalyst with the as-synthesized Nb<sub>2</sub>O<sub>5</sub> and a no-catalyst control experiment (Figure 1). Minimal absorption of NH<sub>4</sub><sup>+</sup> was observed during the one-hour period of stirring in the dark. In the absence of a catalyst, no degradation of NH<sub>4</sub><sup>+</sup> was detected, as expected. The as-synthesized Nb<sub>2</sub>O<sub>5</sub> material was active, albeit weakly, with an apparent first-order rate constant of  $1.6 \times 10^{-3} \text{ min}^{-1}$ . In contrast, the OH-Nb<sub>2</sub>O<sub>5</sub> was ca. 12 times more active, with a rate constant of  $2.0 \times 10^{-2} \text{ min}^{-1}$ . Undesirable nitrate and nitrite byproducts were detected with both the Nb<sub>2</sub>O<sub>5</sub> and OH-Nb<sub>2</sub>O<sub>5</sub> catalysts.

Figure 2 shows the selectivity of nitrite, nitrate, and calculated dinitrogen as a function of ammonium conversion

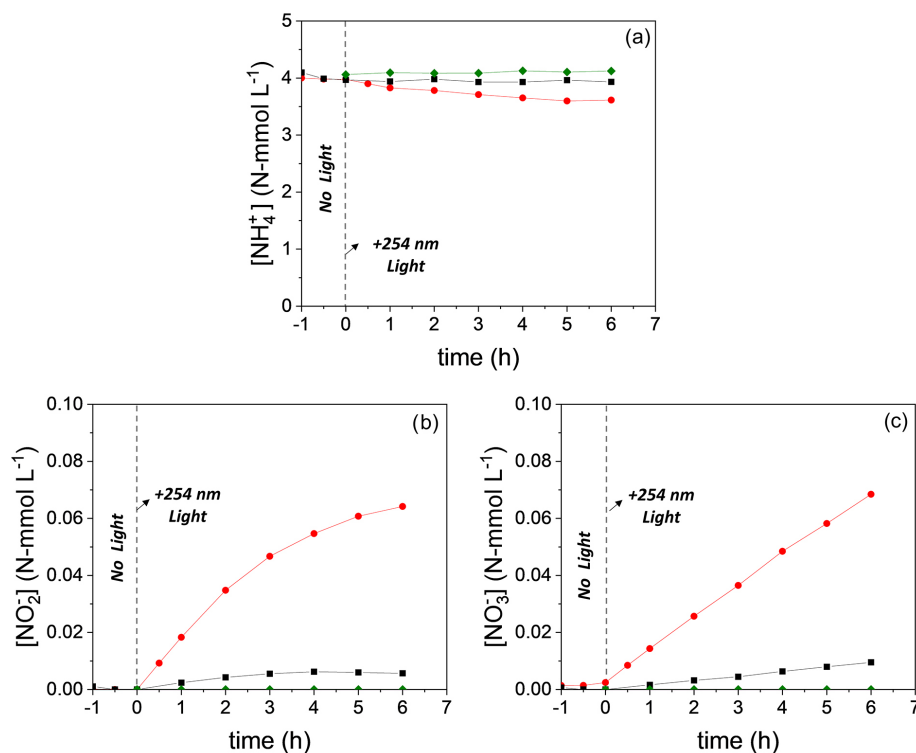


**Figure 1.** (a) Ammonium concentration-time profiles; (b) NO<sub>2</sub><sup>-</sup> concentration-time profiles, and (c) NO<sub>3</sub><sup>-</sup> concentration-time profiles for: no catalyst (—●—), Nb<sub>2</sub>O<sub>5</sub> (—■—), and OH-Nb<sub>2</sub>O<sub>5</sub> (—●—). Reaction conditions: 4 g L<sup>-1</sup> catalyst loading, 600 rpm stirring rate, 1 atm pressure, pH = 9, DI water containing 4.2 mmol N L<sup>-1</sup> NH<sub>4</sub><sup>+</sup> under O<sub>2</sub>-containing headspace.

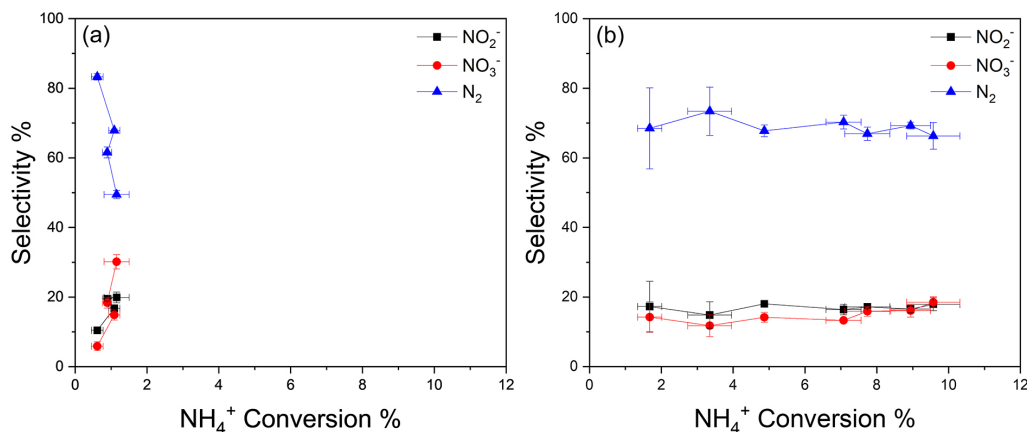


**Figure 2.** Selectivity vs. conversion for (a)  $\text{Nb}_2\text{O}_5$  and (b)  $\text{OH-Nb}_2\text{O}_5$ . Reaction conditions:  $4 \text{ g L}^{-1}$  catalyst loading, 600 rpm stirring rate, 1 atm pressure,  $\text{pH} = 9$ , DI water containing  $4.2 \text{ mmol N L}^{-1} \text{ NH}_4^+$  under  $\text{O}_2$ -containing headspace.

for the two catalysts. In the  $< 1\%$   $\text{NH}_4^+$  conversion range observed,  $\text{Nb}_2\text{O}_5$  had selectivities to nitrite and to nitrate in the range of 20 to 30%, and by nitrogen balance, a  $\text{N}_2$  selectivity of ca. 50%. In the 2–10% conversion range observed, the  $\text{OH-Nb}_2\text{O}_5$  photocatalyst had selectivities to nitrite and to nitrate around ca. 15% and a  $\text{N}_2$  selectivity of ca. 70%. It is tempting to speculate that  $\text{OH-Nb}_2\text{O}_5$  is more  $\text{N}_2$ -selective than  $\text{Nb}_2\text{O}_5$ , but a rigorous comparison of selectivity values cannot be made at different reaction conversions.

We were also interested in comparing the performance of these catalysts to the most used photocatalyst  $\text{TiO}_2\text{-P25}$  under the same reaction conditions used here, as were also published for aqueous photo-oxidation of  $\text{NH}_4^+$ . Vikrant *et al.*<sup>14</sup> proposed the quantum yield (QY) and space-time yield (STY) as a metric to compare photocatalysts that take into account process variables in a unified metric to minimize bias. Based on the QY and STY values for several published photocatalytic materials tested for aqueous photo-oxidation of  $\text{NH}_3/\text{NH}_4^+$ ,  $\text{OH-Nb}_2\text{O}_5$  was more active than the most active material reported thus far (a Pt-modified  $\text{TiO}_2$  catalyst, Table S1, SI section).<sup>14</sup> Moreover, the  $\text{OH-Nb}_2\text{O}_5$  photocatalyst showed 4 fold-times higher ammonia decay rate *per* photon flux (QY) and slightly higher STY than the  $\text{TiO}_2\text{-P25}$  under the same reaction condition and reactor configuration, evidencing the better performance of the  $\text{OH-Nb}_2\text{O}_5$  photocatalyst.

The XRD pattern of the  $\text{OH-Nb}_2\text{O}_5$  and  $\text{Nb}_2\text{O}_5$  structures is very similar to the deformed orthorhombic  $\text{Nb}_2\text{O}_5$  structure reported by Murayama *et al.*,<sup>34,35</sup> with amorphous arrangement in the  $a$ - $b$  plane and crystalline in the  $c$  plane, characteristic of a layered structure. We expected the  $\text{OH-Nb}_2\text{O}_5$  and  $\text{Nb}_2\text{O}_5$  structures to be different, as the alkaline treatment of niobium oxides is known to cause partial dissolution or the formation of alkaline niobate structures.<sup>36,37</sup> No niobate structures were detected via

XRD, as shown by the absence of the corresponding peaks between  $2\theta = 20$  to  $90^\circ$  (Figure 3). Two sharp peaks at  $2\theta = 23.0^\circ$  and  $2\theta = 46.7^\circ$  were present in both samples and attributed to the (001) and (002) planes, respectively, of deformed orthorhombic  $\text{Nb}_2\text{O}_5$  structures. Additionally, the calculated Nb–O–Nb internal layer distance of  $3.86 \text{ \AA}$  is similar to distances reported for  $\text{Nb}_2\text{O}_5$  layered structures.<sup>34,35,38</sup> Notably, the intensity of the detected peaks is much smaller in the  $\text{OH-Nb}_2\text{O}_5$  sample and may indicate much smaller crystalline domains, implying disruption of the bulk crystal structure.

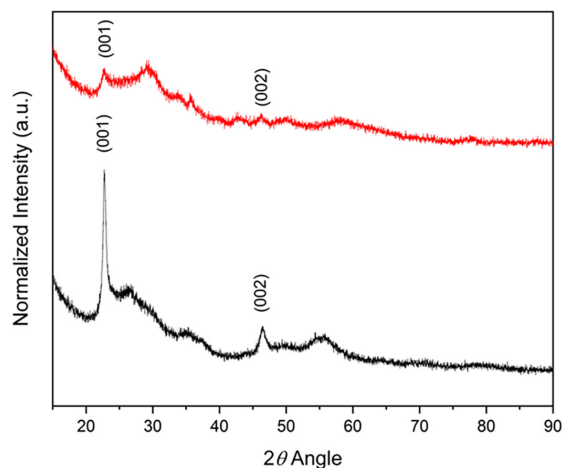


**Figure 3.** X-ray diffraction (XRD) patterns for  $\text{Nb}_2\text{O}_5$  (—) and  $\text{OH-Nb}_2\text{O}_5$  (—).

SEM micrographs and  $\text{N}_2$  physisorption analysis show that the as-synthesized support  $\text{Nb}_2\text{O}_5$  had a fiber-like structure (Figure 4a) with a measured surface area of  $175 \text{ m}^2 \text{ g}^{-1}$ , similar to previously reported semicrystalline  $\text{Nb}_2\text{O}_5$  materials.<sup>34,35,38</sup> Upon treatment with base, the  $\text{Nb}_2\text{O}_5$  structure lost the fiber-like morphology (Figure 4b), and the surface area decreased substantially ( $6 \text{ m}^2 \text{ g}^{-1}$ ). With ca. 30 times less surface area, the  $\text{OH-Nb}_2\text{O}_5$  material

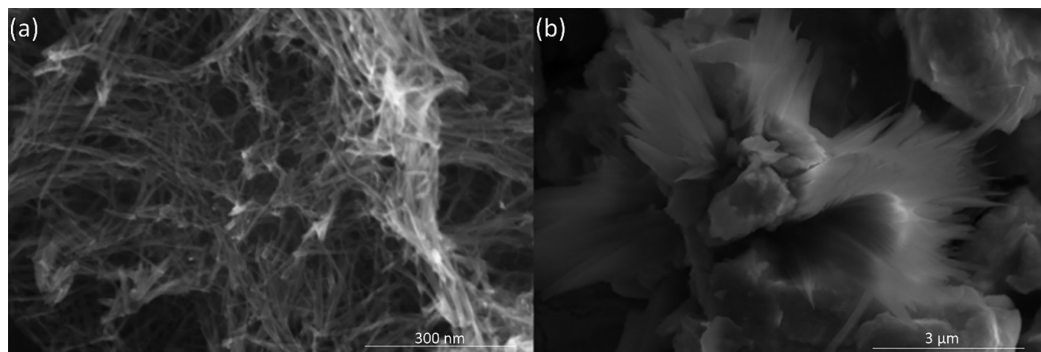


**Figure 4.** SEM micrographs of (a) Nb<sub>2</sub>O<sub>5</sub> and (b) OH-Nb<sub>2</sub>O<sub>5</sub>.

showed ca. 11× higher performance than the Nb<sub>2</sub>O<sub>5</sub> (STY of  $6.29 \times 10^{-3}$  vs.  $5.98 \times 10^{-4}$ , respectively) indicating that the surface area was not the most important contributor for the photo-oxidation performance of the Nb<sub>2</sub>O<sub>5</sub> based materials. Moreover, the difference in the surface area is a strong sign of different surface sites formed after the basic treatment of the Nb<sub>2</sub>O<sub>5</sub> material.

Raman spectroscopy was used to further investigate the photocatalyst structures, as it is commonly used to identify specific polyhedral structures from niobium and oxygen through their different vibrational modes (Figure 5a).<sup>39-41</sup> For Nb<sub>2</sub>O<sub>5</sub>, two bands at 210 and 716 cm<sup>-1</sup> were observed. The shoulder around 283 cm<sup>-1</sup> is from Nb–O stretches in NbO<sub>6</sub> octahedra (Figure 5b). The other two arise from vibrations of Nb–O–Nb bonds, where the former is Nb–O–Nb bending and the latter Nb–O–Nb stretching of corner sharing NbO<sub>6</sub> octahedra in crystalline Nb<sub>2</sub>O<sub>5</sub> (Figure 5c). Moreover, the band at ca. 716 cm<sup>-1</sup> is also indicative of the presence of stretching modes of polyhedral niobium, primarily associated with the orthorhombic phase.<sup>42,43</sup>

The band at 716 cm<sup>-1</sup> was mostly absent in the spectrum for OH-Nb<sub>2</sub>O<sub>5</sub> while a small band appeared at 648 cm<sup>-1</sup>, which is associated with amorphous corner-sharing octahedral NbO<sub>6</sub>, implying the destruction of crystalline corner-sharing Nb–O species after treatment with NaOH.<sup>36,39-41,44-46</sup> The Raman spectrum for OH-Nb<sub>2</sub>O<sub>5</sub> also showed a small but sharp band at 457 cm<sup>-1</sup>, consistent with internal Nb–O stretches of amorphous edge-sharing octahedral NbO<sub>6</sub> (Figure 5d), and an additional band at 533 cm<sup>-1</sup>, consistent with stretching modes of distorted NbO<sub>6</sub> octahedra (Figure 5e). Finally, the appearance of the bands located at 840 and 903 cm<sup>-1</sup> (consistent with the existence of terminal Nb=O bonds, Figures 5f and 5g),<sup>36,47</sup> further corroborates the notion that the crystal structure of Nb<sub>2</sub>O<sub>5</sub> was disrupted by the base treatment.

DR-UV spectroscopy was employed to investigate the potential effects of structural modifications on the semiconductor band gap. Bandgap ( $E_g$ ) energies were determined utilizing Tauc analysis ( $(F(R) hv)^{0.5}$  vs.  $hv$ ), considering the indirect bandgap characteristics inherent

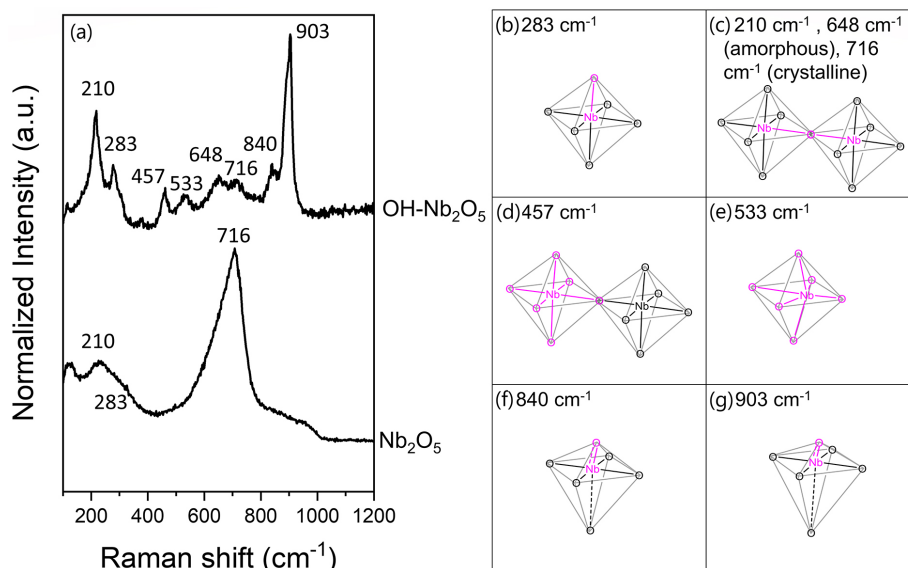


**Figure 5.** (a) *Ex situ* Raman spectra for Nb<sub>2</sub>O<sub>5</sub> and OH-Nb<sub>2</sub>O<sub>5</sub>; and (b-g) niobium octahedra with atoms and lines marked in magenta associated with the Raman vibrational modes.

to both Nb<sub>2</sub>O<sub>5</sub> and OH-Nb<sub>2</sub>O<sub>5</sub>.<sup>28</sup> The calculated bandgap energies for Nb<sub>2</sub>O<sub>5</sub> and OH-Nb<sub>2</sub>O<sub>5</sub> were 3.8 and 4.0 eV, respectively. Remarkably, although the band gaps of the two materials are nearly identical, they both fall below the corresponding UV-C photon energies of 4.9 eV. This intriguing observation suggests that the augmented performance of the OH-Nb<sub>2</sub>O<sub>5</sub> semiconductor is most likely attributed to surface modifications rather than variances in band gap energy.

We hypothesize that the photocatalytic activity of the modified niobium structure is due to the presence of the terminal Nb=O surface sites. At the reaction pH of 9.0 (lower than the pK<sub>a</sub> of NH<sub>4</sub><sup>+</sup>), the majority (ca. 64%) of the NH<sub>3</sub> is expected to be protonated in solution at equilibrium. Both Nb<sub>2</sub>O<sub>5</sub> materials (with a point of zero charge, pzc, around 4.3)<sup>48-50</sup> would be expected to electrostatically adsorb NH<sub>4</sub><sup>+</sup> species since the surface is negatively charged (due to the suspension pH exceeding the pzc). Even though it had a higher surface area, the negligible activity of Nb<sub>2</sub>O<sub>5</sub> highlights the necessity of having Nb=O adsorption sites to promote the photocatalytic reaction (Scheme 1).

Moreover, while higher surface area is usually associated with better adsorption performance, published studies for ammonium/ammonia adsorption using different natural clays reported that a clay with a surface area of 8.45 m<sup>2</sup> g<sup>-1</sup> can adsorb 3 times more NH<sub>4</sub><sup>+</sup> than a clay with 208.93 m<sup>2</sup> g<sup>-1</sup> (ca. 30 fold-times difference), indicating that NH<sub>3</sub>/NH<sub>4</sub><sup>+</sup> adsorption and interaction with a material is not solely dependent on its surface area.<sup>51</sup> Additionally, it

has been reported that surface sites similar to the terminal Nb=O (e.g. O=C=O and C=O) enhance the adsorption of ammonium/ammonia.<sup>31,52</sup>

We speculate that the ammonia photocatalytic oxidation mechanism for OH-Nb<sub>2</sub>O<sub>5</sub> is similar to the mechanism reported for other materials, in which NH<sub>3</sub> (not NH<sub>4</sub><sup>+</sup>) is the species that reacts with hydroxyl radicals (generated through the reaction of holes with water). The resultant partially dehydrogenated NH<sub>m</sub> and NH<sub>n</sub> species (where n and m = 0, 1, or 2) further react with <sup>•</sup>OH or the photogenerated h<sup>+</sup> at the photocatalyst surface for further dehydrogenation and formation of N<sub>2</sub> (equations 7-10). Ammonia may react with hydroxyl radicals to generate hydroxylamine (HONH<sub>2</sub>), which can further react with <sup>•</sup>OH to form NO<sub>2</sub><sup>-</sup> (equation 11). Further oxidation of NO<sub>2</sub><sup>-</sup> to NO<sub>3</sub><sup>-</sup> is proposed to happen in the presence of O<sub>2</sub> (equation 12).<sup>14,31,53</sup> Photogenerated electrons are expected to react with dissolved O<sub>2</sub> to form superoxide species (O<sub>2</sub><sup>-</sup>) and hydroperoxyl radicals (HO<sub>2</sub><sup>•</sup>). Perhaps the Nb=O surface sites can adsorb NH<sub>m</sub> and NH<sub>n</sub> species as surface intermediates, and can also facilitate the N-N coupling needed to form the desired N<sub>2</sub>.

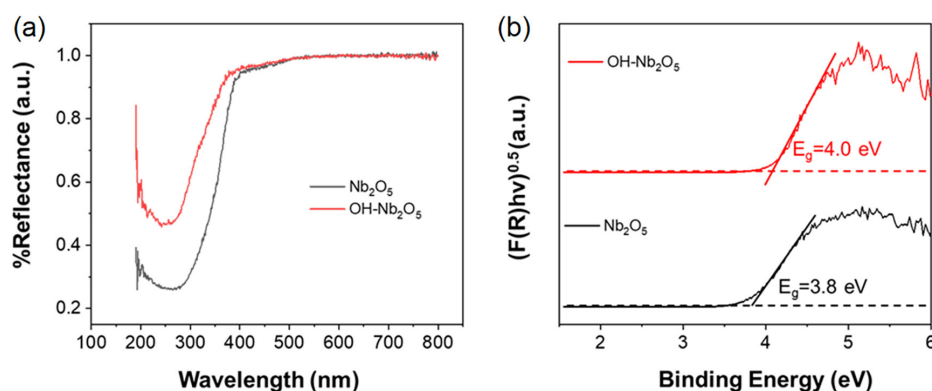
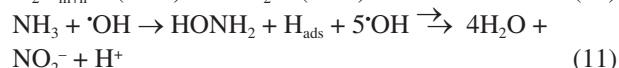
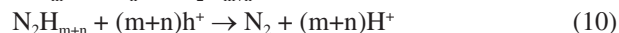
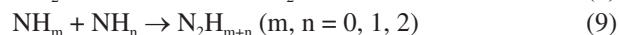
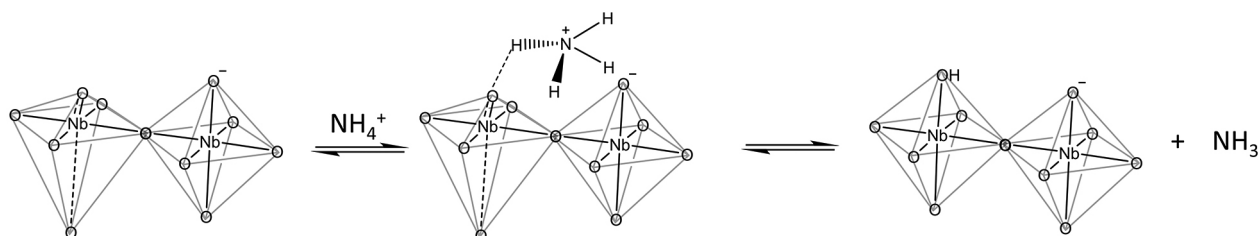


**Figure 6.** (a) DR-UV spectra, and (b) Tauc plots for Nb<sub>2</sub>O<sub>5</sub> and OH-Nb<sub>2</sub>O<sub>5</sub>.



**Scheme 1.** Proposed initial steps of NH<sub>4</sub><sup>+</sup> oxidation catalyzed by OH-Nb<sub>2</sub>O<sub>5</sub>.

## Conclusions

We demonstrate that Nb<sub>2</sub>O<sub>5</sub>, once treated in a basic solution, is active for the photocatalytic oxidation of ammonium under ambient conditions and UV-C irradiation. The modified Nb<sub>2</sub>O<sub>5</sub> photocatalyst was more than ca. 7× active than the most active reported catalysts, which we correlate to the spectroscopically detected Nb=O surface species and not to surface area. These findings suggest that synthesizing Nb<sub>2</sub>O<sub>5</sub> with these surface species and with higher surface areas may lead to more rapid photocatalytic degradation of ammonium and higher selectivity to N<sub>2</sub>.

## Supplementary Information

Supplementary information including results of the pH optimization experiments (Figure S1) and a tabulation of prior photocatalytic studies (Table S1) is available free of charge at <http://jbcbs.sbj.org.br> as PDF file.

## Acknowledgments

The research was sponsored by the Army Research Office (Cooperative Agreement Number W911NF-19-2-0269) and CCDC-ARL (Cooperative Agreement Number W911NF-21-2-0118). The views and conclusions contained in this document are those of the authors and should not be interpreted as representing the official policies, either expressed or implied, of the ARL or the U.S. Government. The U.S. Government is authorized to reproduce and distribute reprints for Government purposes notwithstanding any copyright notation herein. We also acknowledge additional support from the NSF Nanosystems Engineering Research Center for Nanotechnology-Enabled Water Treatment (EEC-1449500). We thank Prof A. Martí and Ms Cecilia Martínez for conducting the DR-UV measurements.

## Author Contributions

Welman C. Elias was responsible for the conceptualization, data curation, formal analysis, investigation, and writing original draft; Chelsea A. Clark for the conceptualization, investigation, visualization, and writing-review and editing; Kimberly N. Heck for the investigation, visualization, and writing-review and editing; Jacob H. Arredondo for the investigation, and writing-review and editing; Bo Wang for the investigation, and writing-review and editing; Andras Toro for the visualization, and writing-review; László Kürti for the visualization, funding acquisition, and writing-review; Michael S. Wong for the project administration, funding acquisition, visualization, writing-review and editing.

## References

- Randall, D. J.; Tsui, T. K. N.; *Mar. Pollut. Bull.* **2002**, *45*, 17. [Crossref]
- Canadian Environmental Protection Act, 1999 and Bills and Related Documents*, <https://www.canada.ca/en/environment-climate-change/services/canadian-environmental-protection-act-registry/related-documents.html>, accessed in October 2023.
- Bernardi, M.; Le Du, M.; Dodouche, I.; Descorme, C.; Deleris, S.; Blanchet, E.; Besson, M.; *Appl. Catal., B* **2012**, *128*, 64. [Crossref]
- Sommer, S. G.; Christensen, M. L.; Schmidt, T.; Jensen, L. S.; *Animal Manure Recycling: Treatment and Management*; John Wiley & Sons, Ltd: Chichester, UK, 2013.
- Zhang, H.; Liu, H.; Zhao, X.; Qu, J.; Fan, M.; *J. Hazard. Mater.* **2011**, *190*, 645. [Crossref]
- van Dongen, U.; Jetten, M. S. M.; van Loosdrecht, M. C. M.; *Water Sci. Technol.* **2001**, *44*, 153. [Crossref]
- The Water Environment Federation (WEF); *Design of Water Resource Recovery Facilities*, 6<sup>th</sup> ed.; McGraw-Hill Education: New York, 2018.
- Zhong, C.; Hu, W. B.; Cheng, Y. F.; *J. Mater. Chem. A* **2013**, *1*, 3216. [Crossref]
- Chmielarz, L.; Jabłońska, M.; *RSC Adv.* **2015**, *5*, 43408. [Crossref]
- Zhu, X.; Castleberry, S. R.; Nanny, M. A.; Butler, E. C.; *Environ. Sci. Technol.* **2005**, *39*, 3784. [Crossref]
- Stathatos, E.; Papoulis, D.; Aggelopoulos, C. A.; Panagiotaras, D.; Nikolopoulou, A.; *J. Hazard. Mater.* **2012**, *211-212*, 68. [Crossref]
- Shavisi, Y.; Sharifnia, S.; Hosseini, S. N.; Khadivi, M. A.; *J. Ind. Eng. Chem.* **2014**, *20*, 278. [Crossref]
- Bonsen, E.-M.; Schroeter, S.; Jacobs, H.; Broekaert, J. A. C.; *Chemosphere* **1997**, *35*, 1431. [Crossref]
- Vikrant, K.; Kim, K.-H.; Dong, F.; Giannakoudakis, D. A.; *ACS Catal.* **2020**, *10*, 8683. [Crossref]
- Hayati, F.; Moradi, S.; Saei, S. F.; Madani, Z.; Giannakis, S.; Isari, A. A.; Kakavandi, B.; *J. Environ. Manage.* **2022**, *321*, 115851. [Crossref]
- Hasanvandian, F.; Moradi, M.; Samani, S. A.; Kakavandi, B.; Setayesh, S. R.; Noorisephehr, M.; *Chemosphere* **2022**, *287*, 132273. [Crossref]
- Mehregan, S.; Hayati, F.; Mehregan, M.; Isari, A. A.; Jonidi Jafari, A.; Giannakis, S.; Kakavandi, B.; *Environ. Sci. Pollut. Res.* **2022**, *29*, 74951. [Crossref]
- Naldoni, A.; D'Arienzo, M.; Altomare, M.; Marelli, M.; Scotti, R.; Morazzoni, F.; Selli, E.; Dal Santo, V.; *Appl. Catal., B* **2013**, *130-131*, 239. [Crossref]
- Sola, A. C.; Ramírez de la Piscina, P.; Homs, N.; *Catal. Today* **2020**, *341*, 13. [Crossref]

20. Nobijari, L. A.; Schwarze, M.; Tasbihi, M.; *J. Nanosci. Nanotechnol.* **2020**, *20*, 1056. [Crossref]
21. Luo, X.; Chen, C.; Yang, J.; Wang, J.; Yan, Q.; Shi, H.; Wang, C.; *Int. J. Environ. Res. Public Health* **2015**, *12*, 14626. [Crossref]
22. Ou, H.-H.; Hoffmann, M. R.; Liao, C.-H.; Hong, J.-H.; Lo, S.-L.; *Appl. Catal., B* **2010**, *99*, 74. [Crossref]
23. Nair, R. V.; Gummaluri, V. S.; Matham, M. V.; C, V.; *J. Phys. D: Appl. Phys.* **2022**, *55*, 313003. [Crossref]
24. Nunes, B. N.; Lopes, O. F.; Patrocinio, A. O. T.; Bahnemann, D. W.; *Catalysts* **2020**, *10*, 126. [Crossref]
25. Marszewski, M.; Cao, S.; Yu, J.; Jaroniec, M.; *Mater. Horizons* **2015**, *2*, 261. [Crossref]
26. Gong, X.; Wang, H.; Yang, C.; Li, Q.; Chen, X.; Hu, J.; *Future Cities Environ.* **2015**, *1*, 12. [Crossref]
27. Lin, M.; An, B.; Niimi, N.; Jikihara, Y.; Nakayama, T.; Honma, T.; Takei, T.; Shishido, T.; Ishida, T.; Haruta, M.; Murayama, T.; *ACS Catal.* **2019**, *9*, 1753. [Crossref]
28. Duan, L.; Wang, B.; Heck, K. N.; Clark, C. A.; Wei, J.; Wang, M.; Metz, J.; Wu, G.; Tsai, A.-L.; Guo, S.; Arredondo, J.; Mohite, A. D.; Senftle, T. P.; Westerhoff, P.; Alvarez, P.; Wen, X.; Song, Y.; Wong, M. S.; *Chem. Eng. J.* **2022**, *448*, 137735. [Crossref]
29. Duan, L.; Wang, B.; Heck, K.; Guo, S.; Clark, C. A.; Arredondo, J.; Wang, M.; Senftle, T. P.; Westerhoff, P.; Wen, X.; Song, Y.; Wong, M. S.; *Environ. Sci. Technol. Lett.* **2020**, *7*, 613. [Crossref]
30. Long, M.; Brame, J.; Qin, F.; Bao, J.; Li, Q.; Alvarez, P. J. J.; *Environ. Sci. Technol.* **2017**, *51*, 514. [Crossref]
31. Liu, D.; Xiu, Z.; Liu, F.; Wu, G.; Adamson, D.; Newell, C.; Vikesland, P.; Tsai, A.-L.; Alvarez, P. J.; *J. Hazard. Mater.* **2013**, *262*, 456. [Crossref]
32. Menezes, B. A. T.; Moreira, D. E. B.; Oliveira, H. A.; Marques, L. F.; Lima, J. F.; *J. Braz. Chem. Soc.* **2020**, *31*, 153. [Crossref]
33. Shavisi, Y.; Sharifnia, S.; Zendezhaban, M.; Mirghavami, M. L.; Kakehazar, S.; *J. Ind. Eng. Chem.* **2014**, *20*, 2806. [Crossref]
34. Murayama, T.; Haruta, M.; *Chin. J. Catal.* **2016**, *37*, 1694. [Crossref]
35. Murayama, T.; Chen, J.; Hirata, J.; Matsumoto, K.; Ueda, W.; *Catal. Sci. Technol.* **2014**, *4*, 4250. [Crossref]
36. Zhu, H.; Zheng, Z.; Gao, X.; Huang, Y.; Yan, Z.; Zou, J.; Yin, H.; Zou, Q.; Kable, S. H.; Zhao, J.; Xi, Y.; Martens, W. N.; Frost, R. L.; *J. Am. Chem. Soc.* **2006**, *128*, 2373. [Crossref]
37. Nico, C.; Monteiro, T.; Graça, M. P. F.; *Prog. Mater. Sci.* **2016**, *80*, 1. [Crossref]
38. Lin, M.; An, B.; Takei, T.; Shishido, T.; Ishida, T.; Haruta, M.; Murayama, T.; *J. Catal.* **2020**, 389, 366. [Crossref]
39. Lopes, O. F.; Paris, E. C.; Ribeiro, C.; *Appl. Catal., B* **2014**, *144*, 800. [Crossref]
40. Santos, I. C. M. S.; Loureiro, L. H.; Silva, M. F. P.; Cavaleiro, A. M. V.; *Polyhedron* **2002**, *21*, 2009. [Crossref]
41. Nowak, I.; Ziolk, M.; *Chem. Rev.* **1999**, *99*, 3603. [Crossref]
42. Braga, V. S.; Dias, J. A.; Dias, S. C. L.; de Macedo, J. L.; *Chem. Mater.* **2005**, *17*, 690. [Crossref]
43. Tiozzo, C.; Bisio, C.; Carniato, F.; Gallo, A.; Scott, S. L.; Psaro, R.; Guidotti, M.; *Phys. Chem. Chem. Phys.* **2013**, *15*, 13354. [Crossref]
44. Zhu, K.; Cao, Y.; Wang, X.; Bai, L.; Qiu, J.; Ji, H.; *CrystEngComm* **2012**, *14*, 411. [Crossref]
45. Brayner, R.; Bozon-Verduraz, F.; *Phys. Chem. Chem. Phys.* **2003**, *5*, 1457. [Crossref]
46. Jehng, J. M.; Wachs, I. E.; *Chem. Mater.* **1991**, *3*, 100. [Crossref]
47. Iliev, M. N.; Phillips, M. L. F.; Meen, J. K.; Nenoff, T. M.; *J. Phys. Chem. B* **2003**, *107*, 14261. [Crossref]
48. dos Santos, A. J.; Batista, L. M. B.; Martínez-Huitle, C. A.; Alves, A. P. M.; Garcia-Segura, S.; *Catalysts* **2019**, *9*, 1070. [Crossref]
49. Shan, Y.; Zheng, Z.; Liu, J.; Yang, Y.; Li, Z.; Huang, Z.; Jiang, D.; *npj Comput. Mater.* **2017**, *3*, 11. [Crossref]
50. Kosmulski, M.; *Langmuir* **1997**, *13*, 6315. [Crossref]
51. Alshameri, A.; He, H.; Zhu, J.; Xi, Y.; Zhu, R.; Ma, L.; Tao, Q.; *Appl. Clay Sci.* **2018**, *159*, 83. [Crossref]
52. Wang, S.; Ai, S.; Nzediegwu, C.; Kwak, J.-H.; Islam, M. S.; Li, Y.; Chang, S. X.; *Bioresour. Technol.* **2020**, *309*, 123390. [Crossref]
53. Lee, J.; Park, H.; Choi, W.; *Environ. Sci. Technol.* **2002**, *36*, 5462. [Crossref]

Submitted: July 6, 2023

Published online: October 10, 2023